Breakup and n-transfer effects on the fusion reactions ^{6,7}Li + ^{120,119}Sn around the Coulomb barrier

M. Fisichella,[1,*] A. C. Shotter,[2] P. Figuera,[1] J. Lubian,[3] A. Di Pietro,[1] J. P. Fernandez-Garcia,[1,4] J. L. Ferreira,[3] M. Lattuada,[1,4] P. Lotti,[5] A. Musumarra,[1,4] M. G. Pellegriti,[1,4] C. Ruiz,[6] V. Scuderi,[1,4] E. Strano,[1,4] D. Torresi,[1,4] and M. Zadro[7]

[1]*INFN, Laboratori Nazionali del Sud, Via S. Sofia 62, I-95123 Catania, Italy*

[2]*School of Physics and Astronomy, University of Edinburgh, JCMB, Mayfield Road, Edinburgh EH9 3JZ, United Kingdom*

[3]*Instituto de Física, Universidade Federal Fluminense, Avenida Litoranea s/n, Gragoatá, Niterói, Rio de Janeiro 24210-340, Brazil*

[4]*Dipartimento di Fisica ed Astronomia, Via S. Sofia 64, I-95123 Catania, Italy*

[5]*INFN, Sezione di Padova, Via F. Marzolo 8, 35131, Padova, Italy*

[6]*TRIUMF 4004 Wesbrook Mall Vancouver, British Columbia V6T 2A3, Canada*

[7]*Ruđer Bošković Institute, Bijenička Cesta 54, HR-10000 Zagreb, Croatia*

(Received 28 July 2016; revised manuscript received 13 December 2016; published 30 March 2017)

This paper presents values of complete fusion cross sections deduced from activation measurements for the reactions ^{6}Li + ^{120}Sn and ^{7}Li + ^{119}Sn, and for a projectile energy range from 17.5 to 28 MeV in the center-of-mass system. A new deconvolution analysis technique is used to link the basic activation data to the actual fusion excitation function. The complete fusion cross sections above the barrier are suppressed by about 70% and 85% with respect to the universal fusion function, used as a standard reference, in the ^{6}Li and ^{7}Li induced reactions, respectively. From a comparison of the excitation functions of the two systems at energies below the barrier, no significant differences can be observed, despite the two systems have different n-transfer Q values. This observation is supported by the results of coupled reaction channels (CRC) calculations.

DOI: 10.1103/PhysRevC.95.034617

I. INTRODUCTION

It has been known for a long time that the fusion cross section of two colliding nuclei is strongly influenced by their mutual interactions as they approach each other [1–4]. At energies below the Coulomb barrier (V_B), these interactions lead to an enhancement of the fusion cross section above the value expected from the one-dimensional barrier penetration model (1D-BPM). The usual way to interpret this is that these mutual interactions excite the participating nuclei to different states just prior to the fusion process. Indeed, it is well known [5,6] that the effect of channel coupling between the ground and excited states is to replace the single fusion barrier by a distribution of barriers extending to energies lower than the one of the single barrier.

The importance of neutron transfer in increasing the sub-barrier fusion probabilities was also suggested, but quantitative understanding of the coupling strengths remained elusive due to the need to rely on complex theoretical calculations. As suggested in [7], the neutron transfer channels could have an important role in nuclear fusion due to the fact that neutrons are insensitive to the Coulomb field and their transfer might start at larger separations than for other particles. This interaction, at separations larger than the sum of nuclei radii, could therefore have an influence on how fusion proceeds. It is expected that, if a colliding system exhibits neutron-transfer channels with positive Q values, the sub-barrier fusion cross section might increase; see, e.g., [7,8]. The idea that neutron transfer processes with a positive Q value would lead to an enhancement of the fusion cross section was also supported by a semiclassical model [9], according to which an intermediate neutron transfer with positive Q value may lead to a gain in relative kinetic energy of the colliding nuclei and, thus, to an enhancement of the barrier penetrability and therefore of the fusion cross section.

Experimental investigations on the neutron transfer effects have often been undertaken by studying similar colliding systems which have different Q values for neutron transfer. For example, enhanced fusion cross sections have been observed for ^{28}Si + ^{94}Zr [10], ^{32}S + ^{96}Zr, ^{110}Pd [11,12] and ^{40}Ca + ^{48}Ca, ^{96}Zr, ^{124,132}Sn [13–16] systems compared to their isotopic counterparts characterized by lower Q values for neutron transfer. However, the fusion excitation functions for systems like Sn+Ni, Te+Ni [17], O+Ge [18], and Ni+Mo [19] do not show significant differences, when different isotopes of the colliding nuclei are considered, even though the systems present very different Q values for multineutron transfer channels. In addition, a recent study concerning the fusion reaction ^{32}S + ^{94}Zr [20] has shown a sub-barrier enhancement with respect to the ^{32}S + ^{96}Zr reaction, [11] although the neutron transfer Q value for ^{32}S + ^{94}Zr is smaller.

A possible solution of this controversy has been proposed using the quantum diffusion approach [21,22]. This study suggests that a sub-barrier enhancement can be related to the neutron transfer process, but this is not directly related to the Q values. The change of the fusion cross section, after the neutron transfer, occurs due to the change of the deformation of the nuclei, which generates a lowering of the Coulomb barrier and consequently an enhancement of the fusion cross section. Therefore, within this approach, in systems where transfer does not modify significantly the deformation of the colliding nuclei there is little effect on the fusion cross section. Similar conclusions were reached in [23].

New measurements, to build up a more complete systematics, are needed for improving the understanding of this

*fisichella@lns.infn.it

TABLE I. Q values (MeV) for $1n$ and $2n$ transfer in the ^{6,7,8,9,11}Li + ^{120,119,118,117,115}Sn collisions.

Reactions	$1n$ stripping	$2n$ stripping
^{6}Li + ^{120}Sn	0.51 MeV	− 12.3 MeV
^{7}Li + ^{119}Sn	1.86 MeV	2.36 MeV
^{8}Li + ^{118}Sn	4.45 MeV	6.30 MeV
^{9}Li + ^{117}Sn	5.26 MeV	9.71 MeV
^{11}Li + ^{115}Sn	9.17 MeV	16.14 MeV

topic. Concerning this issue, the Li+Sn systems are of interest since they have different Q values for neutron transfer (see Table I) and are characterized by a similar nuclear structure. In particular, the target nuclei are spherical due to proton shell closure, and thus the influence of the target inelastic excitation on fusion should be comparable for all the Sn isotopes under investigation, allowing us to better isolate the n-transfer effects.

The compound nucleus formed in the Li+Sn complete fusion (CF) channels listed in Table I is the same for all the systems: ^{126}I. In the reaction energy range around the Coulomb barrier, ^{126}I decays by evaporating mostly neutrons. This is an important feature since it guarantees discrimination between the complete and incomplete fusion (ICF) processes via atomic number identification of the evaporation residues. This is very difficult to achieve in lighter colliding systems where the emission of charged particles is not sufficiently hindered due to the lower Coulomb barrier, so the same evaporation residues are populated both in complete and incomplete fusion reactions. In the present paper results for the ^{6,7}Li + ^{120,119}Sn systems are reported.

The present experimental data can also be used to further investigate the role played by breakup on the fusion process at energies above the Coulomb barrier. At present, it is experimentally well established that the breakup channel hinders complete fusion at energies above the barrier (see, e.g., [4,24–28]). Measurements of fusion with heavy targets, in which low breakup threshold projectiles are involved, have in fact shown a suppression of the CF cross section at energies above the barrier with respect to the one-dimensional barrier penetration model (1D-BPM) or coupled-channel (CC) calculations which do not take coupling to continuum or transfer into account. Such suppression is also observed when the fusion of weakly bound projectiles is compared with that of well bound nuclei on similar targets forming the same compound nucleus (see, e.g., [24] and reference therein). This experimental finding is supported by several calculations (see for example Refs. [29–31]) which predicted that the breakup process generates a dynamic polarization potential whose real part is repulsive, thus producing an increase in the fusion barrier height and consequently a suppression the complete fusion. Although the polarization potential due to breakup is also repulsive at energies below V_B, the CF cross section is enhanced in this energy regime. The explanation for that was recently given by Otomar *et al.* [32]. In that work the authors show that the real part of the dynamic polarization potential of the breakup triggered by one neutron transfer is attractive, and it was assumed that this is the dominant process at energies below V_B. This assumption was based on the experimental data of [33–36].

According to the results reported in the literature, the suppression factor depends on the breakup threshold of the projectile but seems to be almost independent of the mass and charge of the target; see, e.g., [4,28]. Recently, however, studies of reactions induced by ^{6}Li and ^{7}Li on lighter targets such as ^{64}Ni [37,38] and ^{96}Zr [39] have shown suppression factors smaller than the ones reported for instance in the systematics of [28]. For a better understanding of this topic, new measurements of CF with medium and light targets are required, and present data can help in building up a more complete systematics.

The present paper is organised as follows. In Secs. II and III the experimental setup and the procedure used to extract the production cross sections for the evaporation residues will be discussed. In Sec. IV a detailed description of the method used for the determination of the fusion excitation function is given. Then, in Sec. V the experimental results are discussed and compared with CC and coupled reaction channels (CRC) calculations, and other systems previously measured. A summary and conclusions will be given in Sec. VI.

II. EXPERIMENTAL METHODOLOGY

A. Overview

In this work the ^{6}Li + ^{120}Sn and ^{7}Li + ^{119}Sn fusion cross sections were measured by using an activation technique based on the offline detection of the atomic x-rays emitted after the electron capture (EC) decay of the evaporation residues (ER). This technique is particularly suitable for these systems since, according to statistical model calculations, the compound nucleus (^{126}I) decays predominantly by the $3n$ and 2n evaporation channels, thus producing ^{123}I ($t_{1/2}$ = 13 h) and ^{124}I ($t_{1/2}$ = 4 days), decaying by EC into tellurium, which subsequently emits x-rays of 27.3 keV.

The same technique has been used successfully to measure the fusion excitation functions of the systems ^{6,7}Li,^{4,6}He + ^{64}Zn [40–43]. The experimental technique involves two separate stages. First, the targets are irradiated by the beam for a specific period of time. The targets are then removed from the reaction chamber and placed in a low background radiation environment, where the x-rays from the EC decay of the various ERs are monitored over several half-lives. Further details of these two processes are given below.

B. Target activation

The activation step of the measurement was performed in the CT2000 scattering chamber of Laboratori Nazionali del Sud (LNS), with ^{6}Li and ^{7}Li beams delivered by the SMP Tandem accelerator, with an intensity of about 10^{10} pps. In Fig. 1 a schematic representation of the experimental setup used during the activation procedure is shown.

For each bombarding energy, the Li beam first crossed a thin (about 100 μg/cm^2) Au foil and then impinged on a Sn target evaporated onto a catcher foil. The catcher was used to

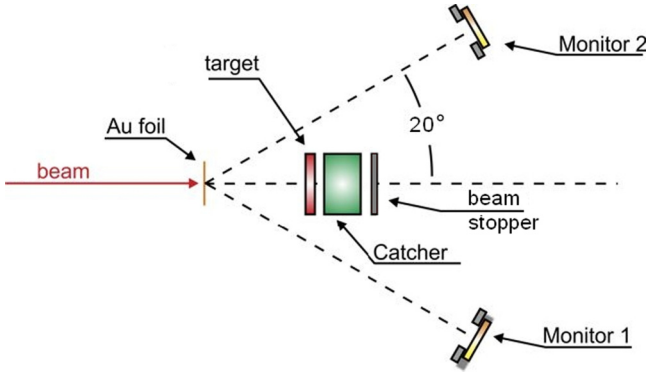

FIG. 1. Sketch of the experimental setup for the activation procedure. The beam passes through a thin Au foil in order to monitor the beam current using Rutherford scattering. A catcher foil follows the Sn target in order to stop recoiling evaporation residuals.

stop the fraction of the ERs which escape from the target. The catcher foils of ^{93}Nb or ^{165}Ho were 2.5 mg/cm^2 thick. After the first runs with Nb catchers, it was realized that the fusion of Li on Nb produced a large background x-ray yield which increased the dead time in the offline counting electronics. Therefore subsequent fusion measurements were undertaken by using the heavier Ho catcher. The typical average thickness of the Sn targets was around 500 μg/cm^2 with a corresponding mean beam energy loss inside the targets of around 200 keV at the bombarding energies of these investigations. Information about the foil thickness and nonuniformity were deduced by measuring residual energy spectra of α particles, emitted by an ^{241}Am source, crossing the foils. A detailed discussion about this procedure will be given in Sec. IV.

The Li beams were collimated by the combination of a 4×4 mm^2 square collimator, placed 156 cm upstream from the Au foil, and a 3.5 mm diameter circular collimator, placed 5 cm upstream from the Au foil. An additional antiscattering collimator was placed 2 cm upstream from the Au foil. In the reaction chamber a target stack holder was mounted on a rotating plate to allow its removal during the beam focusing procedures. In the stack holder, in addition to the stacked foil, a beam stopper was placed in order to prevent the scattered particles emerging from the stack interacting with the monitor detectors.

Since the half-lives of evaporation residuals collected in the target and catcher foils could be comparable to or shorter than the total irradiation time, it was essential to monitor the beam intensity with time. This was accomplished by measuring the elastic scattering of the beam from the thin gold foil, using two 1000 μm surface barrier silicon detectors (see Fig. 1). These two monitor detectors were symmetrically placed at $\pm 20^\circ$ with respect to the beam line, and at a distance of about 80 cm from the Au foil. Since the elastic scattering at this angle follows the Rutherford law, the beam intensity can be extracted by the well known cross-section formula. By using two symmetrical monitors it is possible to reduce systematic errors due to mechanical misalignments and small beam position shifts. The analog-to-digital converters (ADCs) recording events from the detectors also recorded pulser events from a 5 Hz pulser. Since the data were accumulated on an event-by-event basis, the offline analysis could determine the number of elastic scattering events between a specific number of pulser events; from this the corresponding beam intensity vs time profile could be deduced.

The present authors would like to underline that since this paper reports activation results for stable ^{6}Li and ^{7}Li, it would have been possible to perform the whole experiment using single target/catcher foil at each one accelerator beam energy, as outlined in Fig. 1. However it is anticipated that a future experimental program will be undertaken with beams of unstable lithium isotopes ^{8}Li, ^{9}Li, ^{11}Li. Since such beams will be of significantly lower intensity than for stable Li beams, it will be essential to use a stack of target/catcher foils. This will enable several activation measurements at different energies to be simultaneously undertaken with a fixed beam energy. This has already been done in previous similar experiments [40,42,44–50], thus reducing the beam time needed for the measurement. However, using a stack introduces problems which can complicate the interpretation of the activation results. To address this problem a recent publication proposed a new methodology to analyze the raw multiple stack activation data [51]. In order to test some of these ideas, it was therefore decided to use both single target/catcher as well as a stack of them to extract the excitation functions for ^{6}Li + ^{120}Sn and ^{7}Li + ^{119}Sn. This experience should therefore provide a clear pathway to extract accurate fusion excitation functions for radioactive beams where the use of stacks will be unavoidable.

A summary of the different single and multiple target/catcher foils used in this experiment is presented in Tables II and III, along with the mean energy inside the target [see Eq. (5)] and the corresponding measured average cross section.

C. Monitoring of the activated targets

The methodology used to assay the ERs implanted in the target and catcher foils was to measure the x-rays emitted following their EC. Immediately after the end of each activation run, the Sn foil and its associated catcher were taken from the reaction chamber and were moved to the laboratory for the activity measurement, where they were placed in front of a Si (Li) detector. The detector had a diameter of 16 mm, an active thickness of 5 mm, and a Be entrance window 50 μm thick. The Sn foil and associated catcher were placed in a plastic holder to fix their position with respect to the detector, hence reducing the error on the efficiency owing to uncertainties in the geometry. The detector end cup, together with the foil and associated holder, was surrounded by a cylindrical lead shield 5 cm thick. Two identical counting setups were used to follow the decay of the foils for a period of about 6 months after the end of the beam irradiation. As only two targets could be counted at any time, it was necessary to rotate the counting of the various targets so that all irradiated targets could be assayed. Care was taken to ensure all counting sequence had a time stamp so the decay of the ERs through several half-lives could be followed. This timing information was recorded by a 5 Hz pulser being injected into the ADCs recording event-by-event data from

TABLE II. Summary of the targets stacks and single target foils used in the activation experiment with the ^{6}Li beam. The foil thicknesses have been measured by α-particle energy loss. The mean energy inside the target and the corresponding measured average cross sections are also reported.

Setup	E_{mean} lab. (MeV)	Sn thickness (μg/cm^2)	Catcher element	Catcher thickness (mg/cm^2)	σ (mb)
Single	27.9	420	^{93}Nb	1.89	628 ± 49
	26.9	445	^{93}Nb	1.93	507 ± 41
	25.9	475	^{93}Nb	2.41	445 ± 35
	24.9	445	^{93}Nb	2.43	374 ± 29
	21.8	580	^{93}Nb	1.91	133 ± 10
	21.4	455	^{93}Nb	2.45	109 ± 8
	18.6	460	^{93}Nb	2.495	7.46 ± 1.58
	17.3	440	^{93}Nb	2.47	1.31 ± 0.18
Stack 1	24.9	470	^{93}Nb	2.4	381 ± 37
	23.7	480	^{93}Nb	2.4	281 ± 26
	22.5	490	^{93}Nb	2.4	184 ± 17
	21.3	495	^{93}Nb	2.4	101 ± 9
Stack 2	20.8	550	^{93}Nb	1.95	86.3 ± 9.6
	19.7	485	^{93}Nb	1.94	33.1 ± 3.8
	18.6	480	^{93}Nb	1.95	8.50 ± 1.19
	17.4	430	^{93}Nb	1.92	1.67 ± 1.34
Stack 3	17.9	470	^{165}Ho	1.6	2.78 ± 0.21
	17.0	460	^{165}Ho	1.45	0.70 ± 0.05
	16.3	465	^{165}Ho	1.5	0.176 ± 0.030
	15.4	570	^{165}Ho	1.65	0.033 ± 0.011
Stack 4	17.4	460	^{165}Ho	1.5	1.17 ± 0.09
	16.5	575	^{165}Ho	1.42	0.251 ± 0.019
	15.7	565	^{165}Ho	1.5	0.064 ± 0.005
	14.8	610	^{165}Ho	1.45	0.008 ± 0.003

TABLE III. Summary of the target stacks and single target foils used in the activation experiment with the ^{7}Li beam. The foil thicknesses have been measured by α-particle energy loss. The mean energy inside the target and the corresponding measured average cross sections are also reported.

Setup	E_{mean} lab. (MeV)	Sn thickness (μg/cm^2)	Catcher element	Catcher thickness (mg/cm^2)	σ (mb)
Single	27.9	400	^{165}Ho	2.33	692 ± 56
	26.9	485	^{165}Ho	2.30	602 ± 49
	25.9	440	^{165}Ho	2.30	526 ± 4
	24.9	425	^{165}Ho	2.42	468 ± 40
	24.9	420	^{165}Ho	2.33	470 ± 42
	23.7	500	^{165}Ho	2.30	346 ± 30
	22.5	450	^{165}Ho	2.30	240 ± 21
	21.2	482	^{165}Ho	2.42	104 ± 9
	19.7	440	^{165}Ho	2.35	29 ± 2
	18.6	430	^{165}Ho	2.24	7 ± 0.69
	17.3	425	^{165}Ho	2.28	0.84 ± 0.08
Stack 1	17.7	640	^{165}Ho	1.47	1.74 ± 0.13
	16.8	640	^{165}Ho	1.36	0.33 ± 0.03
	15.8	630	^{165}Ho	1.35	0.05 ± 0.01
Stack 2	17.2	540	^{165}Ho	1.3	0.8 ± 0.06
	16.4	510	^{165}Ho	1.49	0.15 ± 0.02
	15.5	520	^{165}Ho	1.43	0.02 ± 0.01

the x-ray detectors; in addition a stopwatch was used to record the start and the stop of the counting cycle of the different target/catcher foil combinations.

The energy calibration of the detectors was undertaken by using the x-rays emitted by ^{55}Fe and ^{109}Cd sources. The detector total efficiency for the 27.30 KeV k_α line of tellurium was determined with the help of Monte Carlo calculations and the use of calibrated x-ray sources of ^{55}Fe (5.86 keV), ^{241}Am (26.34 keV), and ^{137}Cs (32 and 36.32 keV), as described in detail in [52].

III. EXTRACTION OF EVAPORATION RESIDUAL YIELDS

A. Identification of ERs

Following complete fusion of the two reacting nuclei, the excited compound system ^{126}I will deexcite to residual daughter nuclei, by emitting neutrons and gamma rays. At the end of the decay chain, a particular residual nucleus in its ground state could transform further due to subsequent β decay or EC. To determine the total fusion cross section it is necessary to measure the yield of all ERs channels.

According to statistical model codes such as CASCADE [53], the most important evaporation residues for the two studied reactions, accounting for about 95% of the fusion cross section, are ^{124}I and ^{123}I. Both these isotopes decay by EC to tellurium, emitting its k_α and k_β x-rays as a result. As an example, Fig. 2 shows some offline x-ray spectra for ^{6}Li + ^{120}Sn in the energy region of interest, measured at different times after the end of irradiation. It is possible to distinguish the k_α and k_β x-rays produced in the decay of iodine (the only element which can be produced after complete fusion) to tellurium. The analysis of the data was performed only on the k_α lines, taking into account their fluorescence probability. In addition to the tellurium peaks it is also possible to distinguish the k_α and k_β peaks of Sn, produced by the EC decay of Sb. As it will be discussed in Sec. III E, the Sb yield can be due to different reaction mechanisms.

B. Determination of ER yields

As outlined in Sec. II, following beam irradiation of target and catcher foils, two foils would be placed very close to the detector within the lead shield, and the x-ray spectra accumulated for a time t_{a1}, which was significantly shorter than the half-life of the x-ray emitting isotope $\tau_{1/2}$. To enable other foils to be counted, there was a further delay t_{d1}, before the first two foils could be counted for another period t_{a2}. The counting history of any one activated foil was therefore carefully logged as t_0,t_{a1},t_{d1},t_{a2},t_{d2}, . . . ,t_{ai},t_{di}, . . ., with t_0 being the time between the conclusion of the irradiation and the start of the first detector counting period t_{a1}.

All these time periods were determined by a stopwatch. The activity A_{ai} accumulated over time, t_{ai} will correspond to

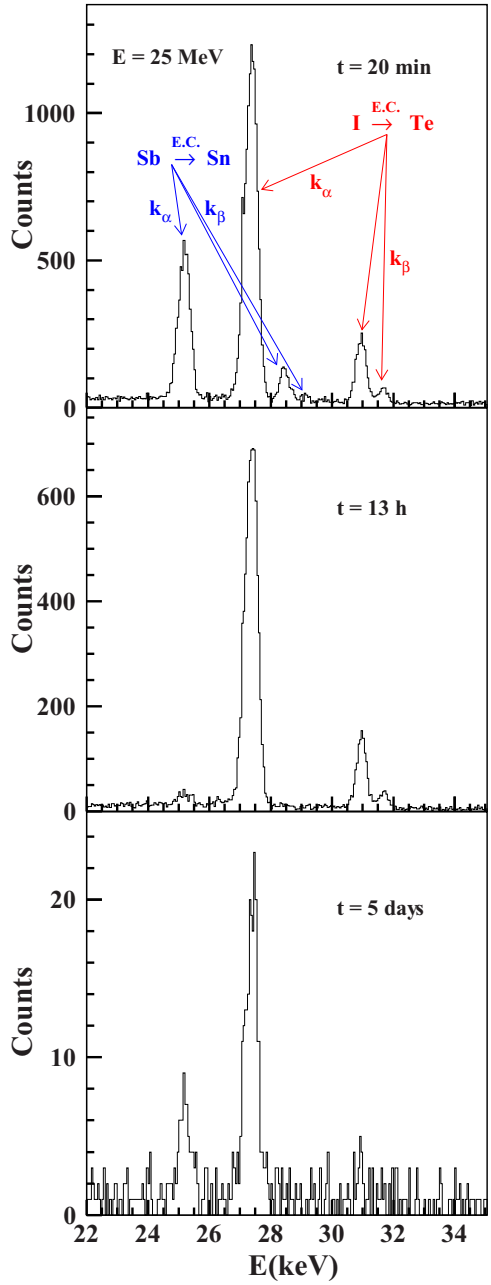

FIG. 2. X-ray spectra measured offline, 20 minutes, 13 hours and 5 days after the end of the irradiation, for the reaction ^{6}Li + ^{120}Sn at 25 MeV. Together with the k_α and k_β x-rays emitted in the EC decay of iodine produced in the CF reactions, it is possible to distinguish the x-rays emitted in the EC decay antimony produced in reactions with the target. See text for details.

a time after target irradiation as T_i where:

$$T_i = \begin{cases} t_0 + \frac{t_{ai}}{2} & i = 1, \\ t_0 + \left[\sum_{n=1}^{i-1}(t_{a_n} + t_{d_n})\right] + \frac{t_{ai}}{2} & i \geqslant 2. \end{cases} \quad (1)$$

The activity was determined from the ratio $N_{ai}/5P_{ai} = A_{ai}$, where N_{ai} is the number of decays, measured during the t_{ai} and P_{ai} the number of events of a 5 Hz pulser, which was also recorded in the ADC, as mentioned above. N_{ai} was obtained

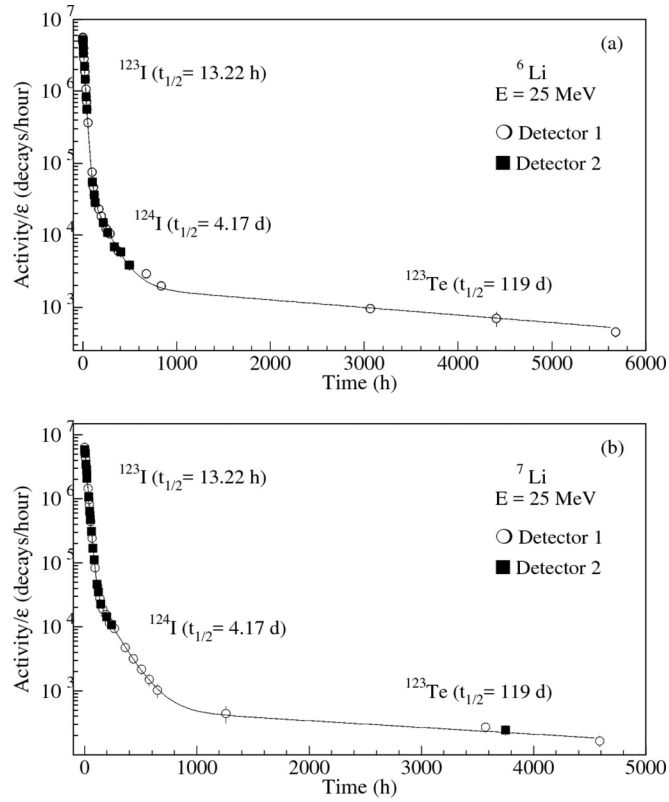

FIG. 3. Typical activity curves (a) for the ^{6}Li + ^{120}Sn reaction and (b) for the ^{7}Li + ^{119}Sn reaction. The continuous line is the best fit of the activity curve.

by subtracting from the total number of counts of the peak of interest the number of background events. The background under the k_α peak has been evaluated by integrating a region near the peak of interest but where there is no evidence of other peaks. In such a way, the average background contribution per channel was extracted and then multiplied by the number of channels where the peak of interest contributes. Since electronic dead-time affects both N_{ai} and P_{ai}, the value of A_{ai} is independent of dead-time.

C. Activity curve analysis

Since the resolution of the x-ray spectra is such that it is not possible to resolve the isotopic shift, the x-ray lines can only identify different elements. However, each isotope contributes to the overall activity with its characteristic half-life, hence the overall activity as a function of the time is the sum of several exponential contributions. This means that contributions of different isotopes can be unfolded by following the activity of the x-ray lines as a function of the time. In Fig. 3 the measured activity corrected for the Si(Li) total efficiency ($\hat{A}_{ai} = A_{ai}/\varepsilon_T$) as a function of total elapsed time, T_i, defined by Eq. (1) is reported for a foil irradiated at 25 MeV in the case of ^{6}Li + ^{120}Sn (top), and ^{7}Li + ^{119}Sn (bottom). The open dots and closed squares represent the data collected by using the two Si(Li) detectors. By looking at these activation curves, it is possible to observe that they are characterised by three different slopes. To identify the isotopes, the activity curve

was fitted with the following function:

$$\hat{A}(t) = \hat{A}_{01}e^{-\lambda_1 t} + \hat{A}_{02}e^{-\lambda_2 t} + \hat{A}_{03}e^{-\lambda_3 t}. \quad (2)$$

The fits have been performed by leaving as free parameters $\hat{A}_{01}, \hat{A}_{02}, \hat{A}_{03}$ and assuming $\lambda_1 = \lambda_{^{123}\mathrm{I}}$ and $\lambda_2 = \lambda_{^{124}\mathrm{I}}$, since ^{123}I and ^{124}I were the residues expected to be produced in the fusion-evaporation process. The third component, was initially assumed to be $\lambda_3 = \lambda_{^{125}\mathrm{I}}$, since ^{125}I could be produced by the evaporation of 1 neutron. However this assumption was not consistent with the decay curve at the high time values. An alternative explanation which fitted the decay curves better, was that the third component corresponds to the decay by internal conversion of the metastable state of ^{123}Te ($11/2^-$, $t_{1/2} = 119$ days) populated in the EC decay of ^{123}I. Moreover, in the case of the ^{6}Li + ^{120}Sn, the ^{123}Te could be also produced by the incomplete fusion of a projectile alpha fragment with the target. The values of $\hat{A}_{01}$, $\hat{A}_{02}$ and $\hat{A}_{03}$ were deduced by the fitting. The $\hat{A}_{01,02,03}$, values correspond to the activity level at the end of the target irradiation.

D. ER production cross section

Once the number of atoms of a given ER isotope at the end of the activation is known, in order to extract the corresponding cross sections, it has to be considered that during the activation, the population of a given isotope is in competition with its decay, if the lifetime of the ERs are comparable to, or shorter than the beam irradiation time t_B. Since in the present case this is true at least for the ^{123}I, it is essential to continuously monitor the beam current, to correct for the decay of the ERs during the irradiation period. To do this a numerical procedure was used. As previously discussed, the number of incident beam particles as a function of time was measured. Using this information, and knowing the thickness of the irradiated foil (i.e., the number of target atoms/cm^2, N_{tar}), the irradiation period, t_B is divided into n equal time intervals Δt. Then the number of ERs of a particular type, identified by index m, at the end of the radiation period is

$$\sigma N_{\mathrm{tar}} \sum_{i=1}^{n} N_{Bi} \exp[-\lambda_m (t_B - i\Delta t)] = \hat{A}_{m0}/\Gamma_m, \quad (3)$$

where N_{Bi} is the number of beam particles interacting with the target over the time period $(i-1)\Delta t$ to $i\Delta t$, and λ_m is the decay constant. On the right-hand side of Eq. (3), the factor Γ_m is equal to $\lambda_m P_{k_\alpha}$, where λ_m is the decay constant of the m isotope, and P_{k_α} is fluorescence probability of the considered isotope. Since the beam history, N_{Bi}, can be deduced by the method outlined in Sec. II, the above equation can be used to deduce σ. The final uncertainties in the cross sections go from about 10% to about 30% depending from the energy, and reflect the statistical and the systematic errors. The contributions to the systematic error are the x-ray detection efficiency (5%), the determination of the beam current (2%), the k_α fluorescence probability (2% for the ^{123}I and 5% for the ^{124}I [54]), and the target thickness (2%). The final systematic error is about 8%.

By comparing the experimental relative yields for the CF residues with the prediction of the statistical model code CASCADE [53], performed by using default input parameters, a good agreement has been observed for both studied reactions. As an example, in Fig. 4 this comparison is shown for some of the measured energies of the ^{6}Li + ^{120}Sn reaction.

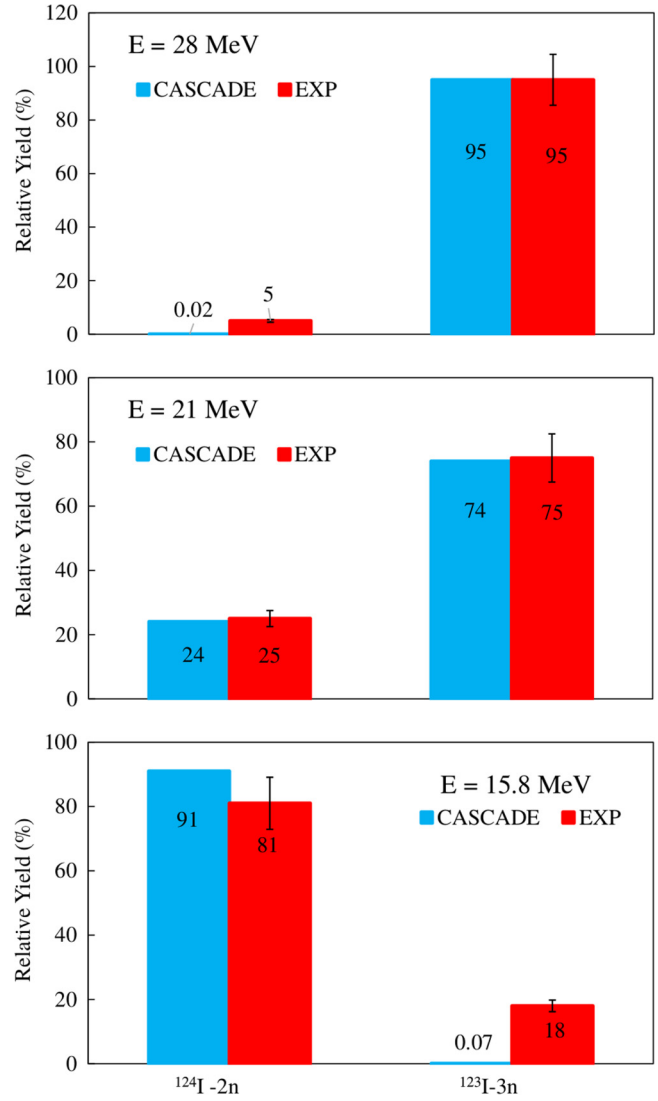

FIG. 4. ER production yields for ^{6}Li + ^{120}Sn at three different energies, compared with the prediction of the statistical model CASCADE [53].

E. Sb production cross section

As shown in Sec. III A, for both reactions at above barrier energies, the x-ray spectra show a yield of Sb which, from the activity curves analysis, has been identified to be ^{120}Sb. This isotope can be produced by different reaction mechanisms. Possible mechanisms contributing to this yield can be the incomplete fusion or a direct cluster transfer of deuterium (for ^{6}Li) and tritium (for ^{7}Li) with the target followed by $2n$ evaporation. In addition ^{120}Sb could also be produced by $1p$ transfer from the projectile. The experimental ^{120}Sb production cross sections measured at above barrier energies are reported in Tables IV and V.

TABLE IV. ^{120}Sb production cross section for the reaction ^{6}Li + ^{120}Sn measured for the energies above the barrier. See text for details.

Incident energy (MeV)	$\sigma_{prod}(^{120}Sb)$ (mb)
21.4	14.9 ± 1.6
21.9	20.5 ± 2.2
22.6	31.9 ± 3.1
23.8	49.9 ± 4.6
25	94.3 ± 8.8
26	120 ± 11
27	134 ± 13
28	156 ± 14

IV. DEDUCTION OF FUSION EXCITATION FUNCTIONS

A. Overview

One of the aims of nuclear reaction studies is often to determine the cross section for a particular reaction process as a function of beam energy, i.e., the excitation function $\sigma(E)$. For the determination of this function a target of finite thickness must be used. The target will produce a reaction yield, Y, from which a mean cross section may be deduced in the usual way, i.e.,

$$\sigma_{\text{mean}} = Y/(N_B N_t), \tag{4}$$

where N_B is the number of beam particles interacting with the target and N_t is the number of target nuclei per unit area. Usually, it is assumed that $\sigma_{\text{mean}} = \sigma(\bar{E})$, where $\bar{E}$ is defined as

$$\bar{E} = \frac{E_0 + E_1}{2}, \tag{5}$$

with E_0 and E_1 being the average beam energies before and after the target, respectively. In other cases [50] it has been assumed that $\sigma_{\text{mean}} = \sigma(E_{\text{eff}})$, where E_{eff} is an effective beam energy defined by weighting the beam energy with the assumed cross section $\sigma(E)$ and the beam energy probability distribution $D(E,t_0)$ inside the target; that is,

$$E_{\text{eff}} = \frac{\int_0^\infty E\sigma(E)D(E,t_0)dE}{\int_0^\infty \sigma(E)D(E,t_0)dE}. \tag{6}$$

Here the $D(E,t_0)$ represents the probability of finding a beam particle with energy E inside a given target with average thickness t_0. However, for thick targets, and/or when the beam entrance energy is not well defined (e.g., if the beam has a large energy dispersion due to interaction with targets upstream in a stack, or because it is a radioactive beam separated in flight), then the above methods of relating σ_{mean} to $\sigma(E)$ can result in misinterpretation of the real excitation function, especially if the cross section is known to vary rapidly over the energy range E_0 to E_1. This situation is thoroughly discussed in [51], where an alternative unfolding procedure is detailed in order to mitigate this problem.

TABLE V. ^{120}Sb production cross section for the reaction ^{7}Li + ^{119}Sn measured for the energies above the barrier. See text for details.

Incident energy (MeV)	$\sigma_{prod}(^{120}Sb)$ (mb)
22.6	98 ± 8.9
23.8	149 ± 13
25	159 ± 15
26	191 ± 17
27	219 ± 20
28	268 ± 25

As discussed in [51], the fusion excitation functions $\sigma(E)$ are generally known to be smooth monotonic functions in the energy region near and below the Coulomb barrier. The measured mean cross sections σ_{mean} are energy mean values of the real excitation function $\sigma(E)$, and can be specified for a particular measurement i by

$$\sigma_{\text{mean},i} = \frac{\int_0^\infty \sigma(E)D_i(E,t_0)dE}{\int_0^\infty D_i(E,t_0)dE}, \tag{7}$$

where the $D_i(E,t_0)$ has the meaning mentioned before. The task is to deduce the continuous function $\sigma(E)$ from a finite number of measured values of $\sigma_{\text{mean},i}$. This may be done by quantifying a suitable function $\hat{g}(E,\mu)$ (with μ parameters to be determined) which shows the same expected energy behavior as $\sigma(E)$, and then minimizing the following expression with respect to μ:

$$S = \sum_i \left(\frac{\sigma_{\text{mean},i} - \hat{g}_{\text{mean},i}}{\beta_i} \right)^2, \tag{8}$$

where

$$\hat{g}_{\text{mean},i} = \frac{\int_0^\infty \hat{g}(E,\mu)D_i(E,t_0)dE}{\int_0^\infty D_i(E,t_0)dE}, \tag{9}$$

and β_i is the experimental error associated with $\sigma_{\text{mean},i}$.

Application of the procedure described above requires detailed knowledge of $D_i(E,t_0)$ which, as described in [51], can be deduced with reasonable reliability with the help of modern codes such as SRIM [55,56]. In general, if the targets are nonuniform, for determining $D_i(E,t_0)$ it is necessary to know the target thickness probability distribution $w(t)$, representing the probability that the incoming particles experience a certain thickness t when crossing a nonuniform target. Although in the present case the beam energy dispersion in the target is small, in the following, the above procedure will be applied as a test case to extract the CF excitation functions for the two studied systems.

It is worth emphasising here that the objective of this procedure is to deduce the best curve $\hat{g}(E,\mu)$, which when convoluted with the $D(E,t_0)$ functions, for each target, reproduces the value of the experimental mean cross sections. So many forms for $\hat{g}(E,\mu)$ may have to be tried before a curve is found that reproduces consistently the experimental values. Moreover, it has to be stressed that the function $\hat{g}(E,\mu)$ is deduced in the laboratory system where the $D(E,t_0)$ functions are calculated.

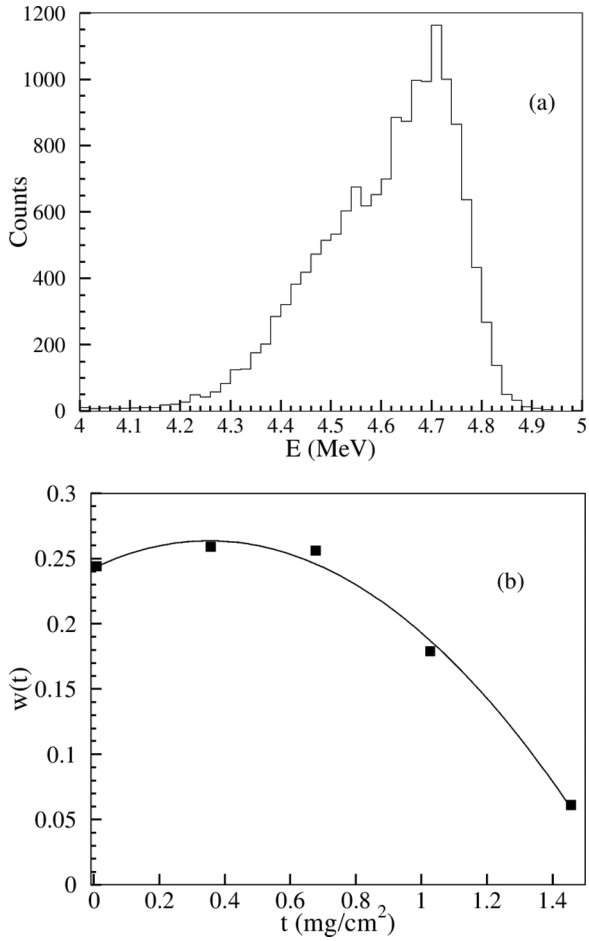

FIG. 5. (a) Typical α-particle residual energy spectrum and (b) the corresponding deduced thickness distribution profile, $w(t)$, for one of the Sn targets.

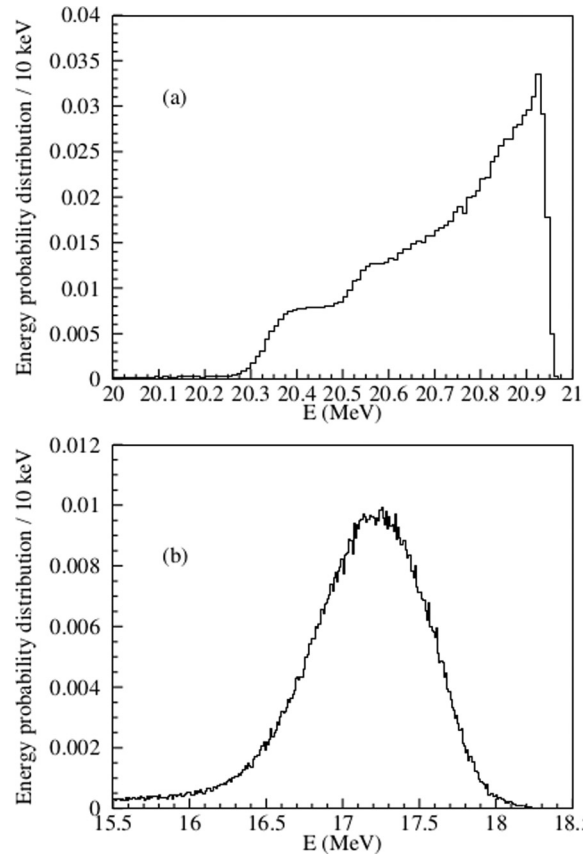

FIG. 6. Beam energy probability distribution $D(E,t_0)$ inside the first (a) and last (b) targets of the second stack (see Table II) in the ^{6}Li + ^{120}Sn reaction.

B. Target thickness probability distribution and $D(E,t_0)$ determination

As noted above, for an accurate determination of the $D(E,t_0)$ function, all the foils used in an activation experiment should be investigated in terms of their thickness distribution. The Sn targets used in the present study were manufactured at LNS-INFN by evaporating ^{119,120}Sn enriched isotopes on rolled ^{93}Nb or ^{165}Ho foils. These targets present important nonuniformities. An investigation with a scanning electron microscope showed that the surface on the Sn side is characterized by structures of different sizes, which vary from some hundreds of nm to about 2 μm [51], which have to be compared with a target average thickness of about 0.7 μm ($\sim$ 500 μg/cm^2).

The thickness distribution for all the targets was determined by using the α-particle transmission method described in [51]. A typical residual energy spectrum of a 5.48 MeV α particles crossing the target, and the associated target thickness probability distribution, $w(t)$, are shown in Fig. 5.

In Fig. 6, as an example, the $D(E,t_0)$ calculated for the first and last foil of the second stack used in the ^{6}Li + ^{120}Sn reaction (see Table II for details) are reported. Note that the beam energy distribution after traversing the first foil of the stack is not Gaussian, as one could expect. The shape of this distribution is dominated by the target nonuniformity, asshown in Fig. 5 for the α-spectra measurements. Concerning the beam distribution of the last foil, its shape is more similar to a Gaussian distribution, but its width is three times wider than the one expected if the foils were uniform. This shape is the result of increased randomization of different thicknesses encountered by the beam as it passes through the upstream targets as compared to the transit of just one foil. Thus, even if a downstream target, i, is quite thin, the presence of upstream target nonuniformity can significantly influence the $D(E,t_0)$ function for the target i. This has to be correctly accounted for in order to reconstruct the fusion excitation functions.

C. Fusion excitation function extraction

Using the experimental mean cross sections extracted for each target i tabulated in Sec. III, and the corresponding calculated $D_i(E,t_0)$, the excitation functions have been extracted using the unfolding procedure summarized above and described in detail in [51]. Several functional forms of $\hat{g}(E,\mu)$ were tried with the aim of discovering a function which, when convoluted with the target $D_i(E,t_0)$, best reproduced the mean measured cross sections. A functional form that is often employed to fit fusion excitation functions is the

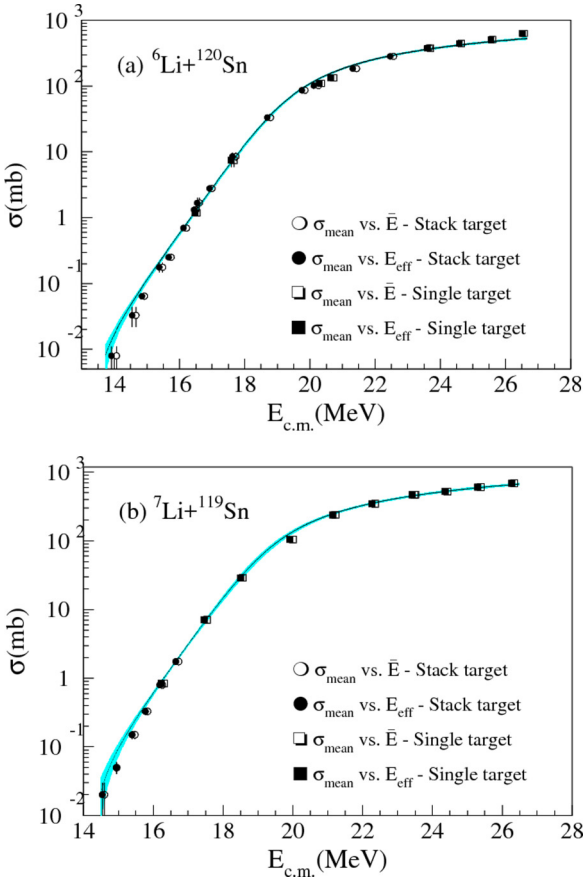

FIG. 7. Fusion excitation function for (a) $^6\mathrm{Li} + {}^{120}\mathrm{Sn}$ and (b) $^7\mathrm{Li} + {}^{119}\mathrm{Sn}$ systems extracted with the deconvolution procedure (continuous line) using the Wong function and its associated uncertainty (colored band). The symbols represent the measured cross sections plotted in the usual way, i.e., as $(\sigma_{\mathrm{mean}}, \bar{E})$ and $(\sigma_{\mathrm{mean}}, E_{\mathrm{eff}})$. Circles are used for points measured with stacked targets and squares are used for single foil measurements. See text for details.

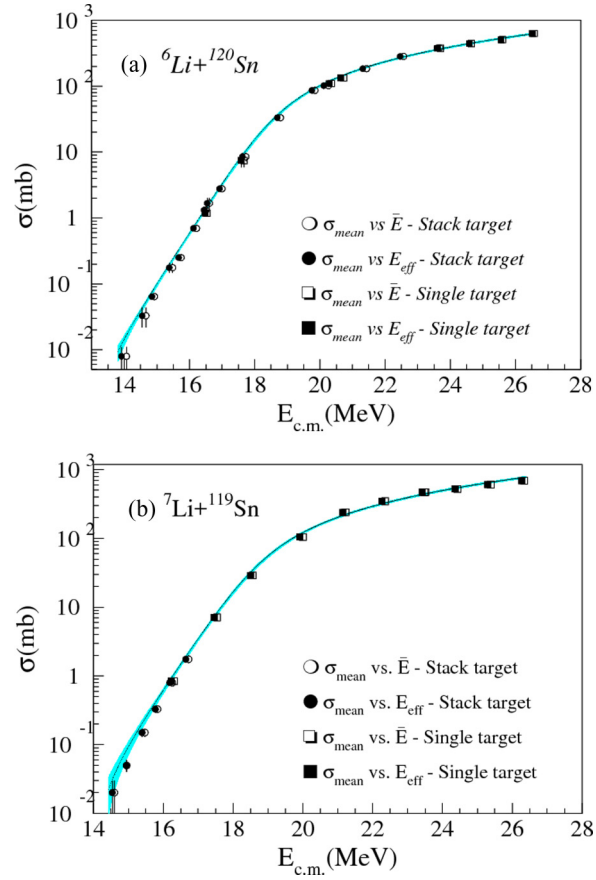

FIG. 8. Fusion excitation function for (a) $^6\mathrm{Li} + {}^{120}\mathrm{Sn}$ and (b) $^7\mathrm{Li} + {}^{119}\mathrm{Sn}$ systems extracted with Eq. (11) (continuous line) and its associated uncertainty (colored band). The symbols represent the measured cross sections plotted in the usual way, i.e., as $(\sigma_{\mathrm{mean}}, \bar{E})$ and $(\sigma_{\mathrm{mean}}, E_{\mathrm{eff}})$. Circles are used for points measured with stacked targets and squares are used for single foil measurements. See text for details.

Wong formula. Therefore, as a first attempt, the Wong formula, expressed as a function of the energy in the laboratory system, was used

$$\hat{g}(E) = \frac{AB}{E} \ln(C + e^{\frac{\pi}{A}(E-D)}) \tag{10}$$

With this expression for $\hat{g}(E,\mu)$, the best parameters to minimise S [Eq. (8)] were $A = 2.00 \pm 0.03$ MeV, $B = 576.74 \pm 22.11$ mb, $C = 0.9999 \pm 0.0004$, $D = 19.85 \pm 0.07$ MeV for the $^6\mathrm{Li} + {}^{120}\mathrm{Sn}$ case and $A = 1.98 \pm 0.03$ MeV, $B = 751.17 \pm 35.71$ mb, $C = 0.9996 \pm 0.0001$, $D = 20.07 \pm 0.01$ MeV for the $^7\mathrm{Li} + {}^{119}\mathrm{Sn}$ case, and E specifies the laboratory energy as used in Eq. (9). The extracted excitation functions for the two systems are shown in Fig. 7 (continuous lines) as functions of the center of mass energy. The shaded area in the figure represents the error band associated with the deconvolution procedure. This error band has been calculated by applying the standard error propagation formula [57] to Eq. (10), considering the four parameters (A, B, C, D) as free variables. This procedure takes account of the error on the single variables as well as possible correlations between the variables of the function through the covariance terms of the error matrix. This deconvolution procedure has been performed by using the MINUIT routine [58], which also provides the error on the parameters and the covariance terms.

Besides the Wong function, other functional forms were tried. For example, a functional form which performed well and gave a lower value of S than the Wong formula was

$$\hat{g}(E) = AE \ln(B + e^{C(E-D)}). \tag{11}$$

Minimizing S [Eq. (8)], the best fit parameters were $A = 1.59 \pm 0.09$ mb MeV^{-1}, $B = 0.9999 \pm 0.0002$, $C = 1.62 \pm 0.04$ MeV^{-1}, and $D = 19.16 \pm 0.08$ MeV for the $^6\mathrm{Li} + {}^{120}\mathrm{Sn}$ case and $A = 2.08 \pm 0.11$ mb MeV^{-1}, $B = 0.9994 \pm 0.0002$, $C = 1.57 \pm 0.04$ MeV^{-1}, and $D = 19.49 \pm 0.08$ MeV for the $^7\mathrm{Li} + {}^{119}\mathrm{Sn}$ case. E specifies the laboratory energy. The extracted excitation functions, obtained for the two systems using Eq. (11), are shown in Fig. 8 as a function of $E_{c.m.}$.

As it will be shown in Sec. V, the barrier parameters associated with the best-fit parameters are comparable with the ones extracted from a double-folding potential.

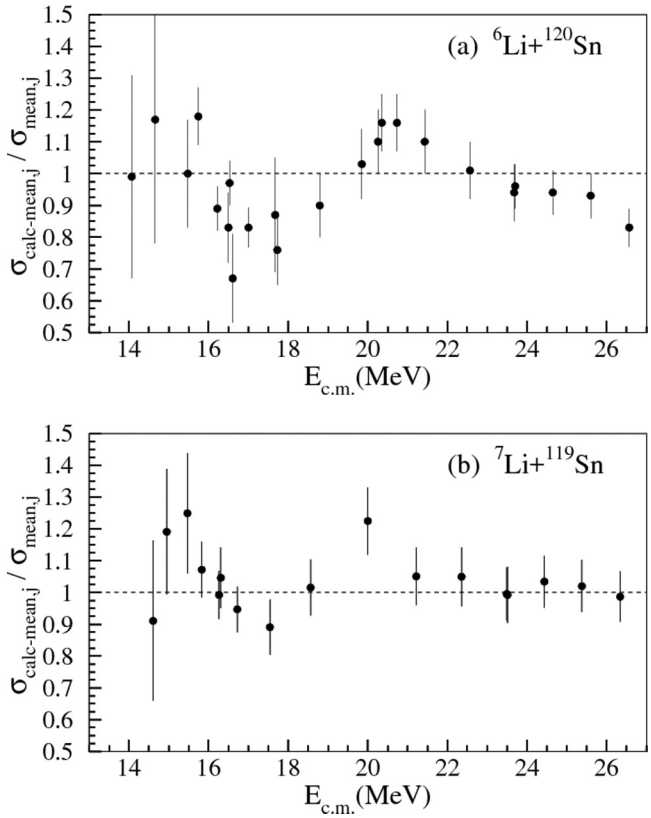

FIG. 9. Ratio between $\sigma_{\text{calc-mean},i}$ and $\sigma_{\text{mean},i}$ for the reactions $^{6}\text{Li} + {}^{120}\text{Sn}$ (a) and $^{7}\text{Li} + {}^{119}\text{Sn}$ (b) using the Wong function. See text for details.

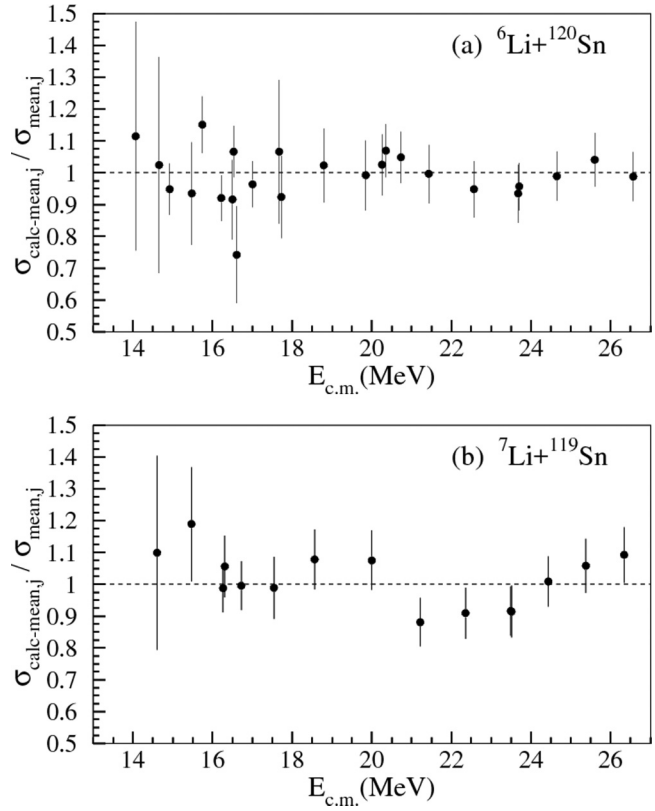

FIG. 10. Ratio between $\sigma_{\text{calc-mean},i}$ and $\sigma_{\text{mean},i}$ for the reactions $^{6}\text{Li} + {}^{120}\text{Sn}$ (a) and $^{7}\text{Li} + {}^{119}\text{Sn}$ (b) using Eq. (11). See text for details.

D. Validation of the functional form used for the extraction of $\sigma(E)$

A crucial point of the deconvolution procedure is the choice of a suitable functional form $\hat{g}(E,\mu)$ able to correctly approximate, with a proper parameter choice, the real excitation function in all the explored energy range. The problem of the suggested approach is that, given a functional form, it will always be possible (from a mathematical point of view) to apply the deconvolution procedure and attain a deconvoluted excitation function, which may differ from the one obtained plotting the measured cross sections as a function of the mean energy. It is therefore mandatory to check if, given a deconvoluted excitation function, the above-mentioned differences are simply due to the fact that the chosen functional form is not able to reproduce the real excitation function, or the differences are, instead, to be attributed to the real effect of the energy spread of the beam. In order to cross-check this, the following self-consistent procedure can be applied. Using the excitation functions extracted with the unfolding procedure, and the calculated $D_i(E,t_0)$, it is possible to calculate the mean cross section that one would measure, for each i, target $\sigma_{\text{calc-mean},i}$ using formula (7). Such a value, for each irradiated target, has to be equal to the corresponding experimental mean cross section $\sigma_{\text{mean},i}$ within the error bars. We applied this procedure both for the Wong function [Eq. (10)] and for Eq. (11). The ratio between $\sigma_{\text{calc-mean},i}$ and $\sigma_{\text{mean},i}$ is reported in Figs. 9 and 10 for the two studied reactions and for the two functional forms respectively. It can be seen that the ratio is fluctuating around unity in the whole energy range for all examined cases, indicating that the whole procedure is self-consistent. However, the variations from unity are larger in the case of the Wong function for which the S values [Eq. (8)] are larger. Systematic effects are observed which depend upon the choice of the deconvolution function. In the case of Eq. (11) these systematic effects are within $\approx\pm 10\%$ and are comparable with the error bars. They are larger in the case of the Wong function. This confirms that Eq. (11) better reproduces the experimental data. Since the ratios in Fig. 10 are all located around 1.0, even for the low energy region, it can be inferred that the differences between the deconvoluted curves in Fig. 8 and the plotted data points are due to beam dispersion effects in the targets. Due to the importance of this observation it will be discussed in more detail below.

E. Deconvolution compared to other extraction methods

Up to the present time, fusion data reported in the literature relating to the analysis of activation experiments, either with single or multiple targets, have presented the excitation function as the best curve through the data points $(\sigma_{\text{mean},i}, \tilde{E}_i)$, where i runs through all the target sets. Some publications identify $\tilde{E}_i$ as the mean energy $\bar{E}$ of the beam as it passes through the target associated with the measurement i, as given by Eq. (5). Other publications associated $\tilde{E}_i$ with the effective

energy $E_{\rm eff}$ defined in Eq. (6). However, as already summarized before and discussed in detail in [51], in general neither $(\sigma_{\rm mean}, \bar{E})$ nor $(\sigma_{\rm mean}, E_{\rm eff})$ will lie on the true $\sigma(E)$ curve. The magnitude of the deviation of the data points from the actual $\sigma(E)$ will depend on the experimental circumstances. For a beam having a well defined energy, and for a small number of thin targets, the deviations will be small. In other cases, for example for thick targets or poor beam quality, the deviations could be significant and even lead to serious misinterpretation of the data [51]. In the present case these effects were expected to be small, but the procedure was applied as a test case and indeed differences in the exponential region, although small, are significant.

Inspection of Fig. 8 shows that the data set $(\sigma_{{\rm mean},i}, \bar{E})$ or $(\sigma_{{\rm mean},i}, E_{\rm eff})$ do deviate at lower energies from the σ(E) extracted with the deconvolution procedure represented by the continuous line, as mentioned in the previous paragraph. Also it can be seen that for a particular $\sigma_{{\rm mean},i}$, data plotted either using $\bar{E}$ or $E_{\rm eff}$ do not coincide.

According to the results discussed in [51], it is opinion of the present authors that these effects could be more important in the study of the reactions induced by unstable beams listed in Table I. In those cases it will be essential to carefully determine all the relevant $D(E,t_0)$ functions and apply the deconvolution procedure rather than relying on $\bar{E}$ and $E_{\rm eff}$ to extract the fusion excitation functions. Another important point to emphasise here is the significance of the deduced "best function" from data set. The deconvolution procedure to identify the best function is an analysis device to determine the function which is the best surrogate of the actual cross section. However, this function will have no validity to represent the cross section outside the energy data range from which it was deduced.

V. COMPARISON OF THE DATA WITH THEORETICAL PREDICTIONS AND DISCUSSION

In this section the measured CF cross sections of the ^{6}Li + ^{120}Sn and ^{7}Li + ^{119}Sn will be compared with the theoretical predictions of coupled channels (CC) calculations involving inelastic excitation channels and, in the final part of Sec. V B also n-transfer channels, but always excluding breakup channels. The idea is that any difference between the theoretical predictions and experimental cross-section values could be attributed to other channels not included in CC calculations.

A. Complete fusion suppression above the barrier

As already mentioned in the introduction, the existing CF experimental data show a suppression of the measured fusion cross sections with respect to the 1D-BPM and/or the CC calculations which do not take coupling to continuum or transfer into account (see [4] and references therein). It is quite clear that the suppression factor depends on the breakup threshold of the projectile (see, e.g., [4]): it is smaller for the ^{7}Li (breakup threshold 2.47 MeV) induced reactions with respect to the ones induced by ^{6}Li (breakup threshold 1.47 MeV). Moreover, the ^{7}Li nucleus has one bound excited state that competes with the breakup channel, while ^{6}Li has only one bound state, i.e., the ground state. An aspect, not completely clarified, is the target mass (and/or charge) dependence of the suppression factor due to breakup.

To make further progress in the understanding of complete fusion, Wang *et al.* [28] performed a systematic comparison of the existing experimental data by using a reduction procedure, introduced by Canto *et al.* [25,26], based on the Wong approximation [59] for the fusion cross section. According to this reduction procedure, which factors out the trivial static effects due to geometry, the collision energy and the experimental fusion cross section are reduced as follows:

$$E_{c.m.} \rightarrow x = \frac{E_{c.m.} - V_B}{\hbar\omega}, \tag{12}$$

$$\sigma_F \rightarrow F(x) = \frac{2E_{c.m.}}{\hbar\omega R_B^2}\,\sigma_F, \tag{13}$$

where V_B, R_B, and $\hbar\omega$ represent the height, radius, and curvature of the Coulomb barrier. In this kind of reduction, in order to disentangle the effect of one or more reaction channels, and/or to eliminate the inaccuracies of the Wong approximation at energies below and above the barrier, a renormalized fusion function is usually introduced [25,26]:

$$\bar{F}_{\rm exp}(x) = F_{\rm exp}(x)\,\frac{\sigma_F^W}{\sigma_F^{CC}}, \tag{14}$$

where σ_F^W is the Wong cross section, and σ_F^{CC} is the fusion cross section of a CC calculation which includes all channels, except the ones for which their effects on fusion cross section are the subject of study. In the present case the CC at energies above the barrier is small and the values of the suppression factors derived without the renormalization are practically the same. Nevertheless a decision was made to follow the full Canto renormalisation procedure to keep a formal uniformity for comparison with other systems where this correction could be important. This is usually the case at energies below the barrier. Once the data are normalized, the CF suppression factor is then extracted by comparing the reduced data with a benchmark function, the universal fusion function (UFF), defined as [25,26]

$$F_0(x) = \ln[1 + \exp(2\pi x)], \tag{15}$$

which is obtained applying the transformations of Eqs. (12) and (13) to the Wong formula [59] for the fusion cross section. In an ideal situation where coupling effects are fully contained in the CC calculations, $\bar{F}_{\rm exp}(x)$ is identical to the UFF. The parameters of the Coulomb nominal barrier used in the reduction procedure were $R_B = 10.34$, $V_B = 19.48$ MeV, and $\hbar\omega = 3.82$ MeV for the ^{7}Li + ^{119}Sn system and $R_B = 10.18$ fm, $V_B = 19.74$ MeV, and $\hbar\omega = 4.16$ MeV for the ^{6}Li + ^{120}Sn system. These parameters were derived using the São Paulo potential. It should be pointed out that these parameters correspond to the nominal Coulomb barrier derived using a bare potential. In general, if a Wong-like formula is used to reproduce experimental fusion excitation functions, the obtained barrier parameters correspond to an average experimental barrier which includes effects of the coupling to all reaction channels. As a consequence, in general, if

the experimental data are strongly affected by the coupling to different reaction channels, the parameters related to the nominal barrier may differ from the ones obtained by fitting the data. In the present case the values of the barrier parameters in Eq. (11) are similar to the one obtained from the São Paulo potential.

In their systematics Wang *et al.* [28] show that the data concerning collisions induced by ^{6}Li on ^{90}Zr, ^{144}Sm, ^{152}Sm, ^{159}Tb, ^{198}Pt, and ^{209}Bi are suppressed with respect to the UFF by factor 0.60, whereas data for collisions induced by ^{7}Li on ^{144}Sm, ^{152}Sm, ^{159}Tb, ^{165}Ho, ^{198}Pt, and ^{209}Bi are suppressed with respect to the UFF by a factor 0.67. The suppression factor is defined as the value for which the benchmark function has to be multiplied to reproduce the data.

For the sake of comparison with the previously measured systems, the present authors used the reduction procedure of [25,26] to determine the CF suppression factors of the ^{6}Li + ^{120}Sn and ^{7}Li + ^{119}Sn systems. The data set used for this procedure has been obtained from the deconvolution curve shown, as a continuous line, in Fig. 8. The data sets are $(\sigma_{\mathrm{mean},i}, E_{\mathrm{dec},i})$, where $E_{\mathrm{dec},i}$ is the energy point of the deconvolution curve which corresponds to the measured cross section $\sigma_{\mathrm{mean},i}$. In Fig. 11 the renormalized fusion function value $\bar{F}_{\mathrm{exp}}(x)$, Eq. (14), is plotted, for the two data sets reported in Fig. 8. The full curve in Fig. 11 corresponds to the benchmark function UFF.

In all calculations of the present work, the FRESCO code was used [60]. In the CC calculations, performed to obtain the renormalized fusion functions defined in Eq. (14), since there is no bound excited state for the ^{6}Li projectile, only its g.s. was included in the coupling scheme. ^{6,7}Li resonance states were not included in the coupling scheme, since the effect of the whole continuum on the CF cross section was under investigation. In the case of the ^{7}Li projectile the quadrupole coupling to the first bound excited state $1/2^{-}$ at 0.4776 MeV was included. Concerning the target excitations, the quadrupole excitations of the $3/2^{+}$ and $5/2^{+}$ at 0.0239 and 0.9214 MeV, respectively, of ^{119}Sn and the 2^{+} one-phonon and the triplet of two-phonons (0^{+}, 2^{+}, and 4^{+}) states of ^{120}Sn at 1.1714, 1.8751, 2.0972, and 2.1943 MeV, respectively, were all included. The quadrupole deformation parameters β_2 were taken from the systematics [61].

The real part of the optical potential corresponds to the parameter-free double folding São Paulo potential [62,63]. At near barrier energies this potential is a usual double folding potential with the advantage that it has a comprehensive systematics for the matter densities. This potential was the one used to obtain the systematics in Refs. [25,26,28,64], and in other works found in the literature. It is important to use the same potential because, although the qualitative results may be the same using other potentials, the quantitative results might be slightly different [65]. For the imaginary part of the optical potential, a Woods-Saxon potential with the parameters $W_0 = -50$ MeV, $r_w = 1.06$ fm and $a_w = 0.2$ fm for the depth, reduced radius, and diffuseness, respectively, was used. This choice of the parameters guarantees that the absorption occurs only after the impinging nucleus is inside the Coulomb barrier.

In the upper (a) panel of Fig. 11, the CF reduced cross sections are shown in a logarithmic scale that is more appropriate for studying the cross sections at energies below the Coulomb barrier [$x = 0$, according to Eq. (12)]. On the other hand, the lower (b) panel in linear scale is more appropriate for $E_{c.m.} > V_B$ ($x > 0$). From Fig. 11, it can be seen that by comparing the experimental reduced fusion cross section with the UFF, for both the reactions, the CF is enhanced at energies below V_B and hindered above it, due to the effect of breakup plus transfer channels (these were the reaction channels left out in the CC calculations used to renormalize the data) in agreement with the results of Refs. [25,26,28]. When account of the systematic error is taken, the suppression factor for the ^{6}Li + ^{120}Sn system is determined to be 0.70 ± 0.05, and for the ^{7}Li + ^{119}Sn system it is 0.85 ± 0.05. Such values, while confirming the breakup threshold dependence of the suppression factors, appear to be slightly nearer to unity than the ones found in the systematics of Wang *et al.* [28].

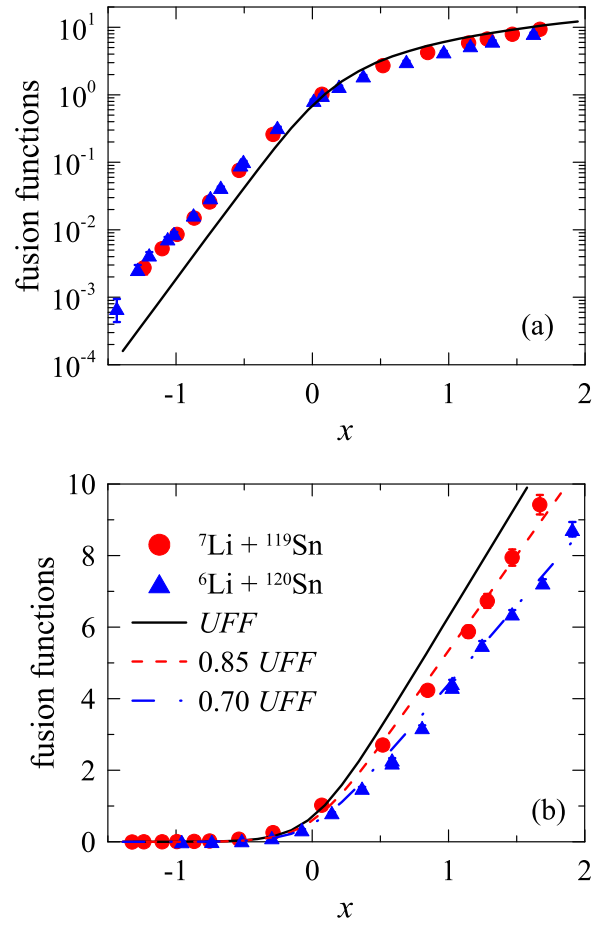

FIG. 11. Comparison of CF reduced cross section for the ^{6}Li + ^{120}Sn and ^{7}Li + ^{119}Sn systems with the UFF. The experimental data reported in the figure correspond to $(\sigma_{\mathrm{mean},i}, E_{\mathrm{dec},i})$, where $E_{\mathrm{dec},i}$ is the energy point of the deconvolution curve which corresponds to the measured cross section $\sigma_{\mathrm{mean},i}$. See text for details.

It has to be noticed that recently, suppression factors even closer to unity than the ones reported in this paper have been deduced for the following systems with lighter targets: ^{6}Li + ^{64}Ni (0.87) [37], ^{7}Li + ^{64}Ni (0.94) [38], and ^{6}Li + ^{96}Zr (0.75) [66]. To establish a definitive dependence

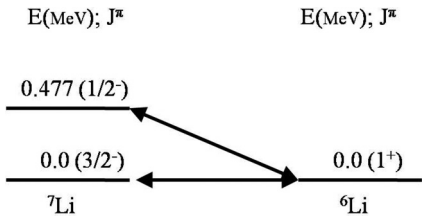

FIG. 12. Couplings scheme for the projectile overlaps.

of the suppression factor with target mass, it would be valuable to undertake experiments measuring CF for ^{6}Li and ^{7}Li across a range from the light ^{12}C to the heaviest ^{208}Pb. Unfortunately, however, a clear separation of CF and ICF is not experimentally easy to obtain for light systems since, due to charged-particle evaporation, CF and ICF populate the same evaporation residues.

B. Complete fusion below the barrier and n-transfer effects

At energies below the barrier, as already observed in collisions of ^{6,7}Li with different targets (see, e.g., [4]), the UFF underestimates the data; this shows the combined effect of the coupling to continuum and transfer channels not explicitly taken into account in CC calculations used to renormalize the data. However, it is interesting to note with respect to the aim of the present work that the two sets of reduced data (Fig. 11) are very close in spite of the different n-transfer Q values. This behavior seems to be consistent with the one observed in fusion reactions of heavier systems [17–19] and appears to confirm the idea, proposed in [21–23], that it is not just the difference in the n-transfer Q value itself which generates a modification of the behavior of the fusion cross section.

In order to have a better idea of the effect of n transfer on the fusion cross sections, finite-range coupled reaction channels (CRC) calculations for the $1n$ stripping reaction ^{119}Sn(^{7}Li,^{6}Li)^{120}Sn have been performed. For these calculations, the double-folding São Paulo potential was also used for the real part of the optical potential of the entrance and exit partitions [62,63]. The imaginary part for the entrance partition (^{7}Li + ^{119}Sn) was considered to be of the Woods-Saxon form with parameters $W = -50.0$ MeV, $r_w = 1.06$ fm, and

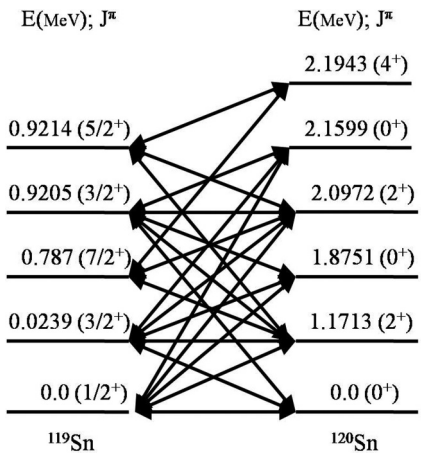

FIG. 13. Couplings scheme for the target overlaps.

TABLE VI. Spectroscopic amplitudes for projectile overlaps ($\langle^7$Li$|^6$Li$\rangle$) using ^{4}He as core.

Initial state	J	Final state	Spec. amp.
^{7}Li$_{g.s}(3/2^-)$	$1p_{1/2}$	^{6}Li$_{g.s}(1^+)$	0.538
	$1p_{3/2}$	^{6}Li$_{g.s}(1^+)$	0.657
^{7}Li$_{0.478}(1/2^-)$	$1p_{1/2}$	^{6}Li$_{g.s}(1^+)$	−0.196
	$1p_{3/2}$	^{6}Li$_{g.s}(1^+)$	−0.924

$a_w = 0.2$ fm for the depth, reduced radius, and diffuseness, respectively; these parameters are the same as those used for the CC calculations discussed in Sec. V A. The prior approximation was used, and the nonorthogonal corrections and full complex remnant were taken into account. For the final partition (^{6}Li + ^{120}Sn), the São Paulo potential was used for both real and imaginary parts with strength coefficients $N_R = 1.0$ and $N_I = 0.78$, respectively. This approach has proved to be suitable for describing the elastic scattering cross sections for several systems [67] in a wide energy interval. In the entrance partition the collective states of the projectile and target were also considered, as described in Sec. V A.

The spectroscopic amplitudes for both projectile and target overlaps were obtained from shell-model calculations using

TABLE VII. Spectroscopic amplitudes for target overlaps ($\langle^{119}$Sn$|^{120}$Sn$\rangle$) with ^{116}Sn as closed core.

Initial state	J	Final state	Spec. amp.
^{119}Sn$_{g.s}(1/2+)$	$3s_{1/2}$	^{120}Sn$_{g.s}(0^+)$	−1.323
	$2d_{3/2}$	^{120}Sn$_{1.171}(2^+)$	0.263
	$3s_{1/2}$	^{120}Sn$_{1.875}(0^+)$	−0.131
	$2d_{3/2}$	^{120}Sn$_{2.097}(2^+)$	−0.021
	$3s_{1/2}$	^{120}Sn$_{2.160}(0^+)$	0.390
^{119}Sn$_{1.581}(3/2+)$	$2d_{3/2}$	^{120}Sn$_{g.s}(0^+)$	−0.570
	$3s_{1/2}$	^{120}Sn$_{1.171}(2^+)$	−0.822
	$2d_{3/2}$	^{120}Sn$_{1.171}(2^+)$	−0.178
	$2d_{3/2}$	^{120}Sn$_{1.875}(0^+)$	0.698
	$3s_{1/2}$	^{120}Sn$_{2.097}(2^+)$	0.009
	$2d_{3/2}$	^{120}Sn$_{2.097}(2^+)$	0.042
	$2d_{3/2}$	^{120}Sn$_{2.160}(0^+)$	−1.094
^{119}Sn$_{1.750}(7/2+)$	$2d_{3/2}$	^{120}Sn$_{1.171}(2^+)$	−0.365
	$3s_{1/2}$	^{120}Sn$_{2.097}(2^+)$	0.170
	$2d_{3/2}$	^{120}Sn$_{2.194}(4^+)$	0.861
	$2d_{3/2}$	^{120}Sn$_{2.194}(4^+)$	0.094
^{119}Sn$_{2.225}(3/2+)$	$2d_{3/2}$	^{120}Sn$_{g.s}(0^+)$	0.375
	$3s_{1/2}$	^{120}Sn$_{1.171}(2^+)$	−0.220
	$2d_{3/2}$	^{120}Sn$_{1.171}(2^+)$	−0.145
	$2d_{3/2}$	^{120}Sn$_{1.875}(0^+)$	0.220
	$3s_{1/2}$	^{120}Sn$_{2.097}(2^+)$	0.165
	$2d_{3/2}$	^{120}Sn$_{2.097}(2^+)$	−0.035
	$2d_{3/2}$	^{120}Sn$_{2.160}(0^+)$	1.172
^{119}Sn$_{2.438}(5/2+)$	$3s_{1/2}$	^{120}Sn$_{1.171}(2^+)$	0.966
	$2d_{3/2}$	^{120}Sn$_{1.171}(2^+)$	−0.394
	$3s_{1/2}$	^{120}Sn$_{2.097}(2^+)$	0.280
	$2d_{3/2}$	^{120}Sn$_{2.194}(4^+)$	0.045
	$2d_{3/2}$	^{120}Sn$_{2.194}(4^+)$	0.198

TABLE VIII. Comparison of experimental data and NUSHELLX results for the ^{6,7}Li and ^{119,120}Sn spectra.

Nucleus	Interaction	J^π	$E_{\rm exp}$	$E_{NuShellX}$	Δ E
^{6}Li	cki	1^+	0.0	0.0	0.0
^{7}Li	cki	$3/2^-$	0.0	0.0	0.0
		$1/2^-$	0.477	1.068	−0.591
^{119}Sn	sn100pn	$1/2^+$	0.0	0.0	0.0
		$3/2^+$	0.024	0.229	−0.205
		$7/2^+$	0.787	0.660	0.127
		$3/2^+$	0.9205	0.801	0.120
		$5/2^+$	0.9214	0.862	0.059
^{120}Sn	sn100pn	0^+	0.0	0.0	0.0
		2^+	1.171	0.379	0.792
		0^+	1.875	1.419	0.456
		2^+	2.097	1.096	1.001
		0^+	2.160	1.671	0.489
		4^+	2.194	0.842	1.352

the NUSHELLX code [68]. For ^{7}Li, the effective interaction "cki" [69] was used for the valence protons and neutrons in the $1p_{3/2}$ and $1p_{1/2}$ orbits, and considering the α particle as a closed core. For the ^{119}Sn, the effective interaction sn100pn [70] was used, and valence neutrons in the orbits $2d_{3/2}$, $3s_{1/2}$, and $1h_{11/2}$ were taken into account. ^{116}Sn was considered as a closed core. In Figs. 12 and 13 the projectile and target coupling schemes considered in the calculations are sketched. We verified that adding the long lived 3^+ state of ^{6}Li at 2.186 MeV in the coupling scheme of Fig. 12 does not change the results of the calculations.

In Tables VI and VII the results of NUSHELLX predictions for the spectroscopic amplitudes are shown. In Table VIII a comparison of the corresponding experimental spectra for ^{7}Li, ^{6}Li, ^{119}Sn, and ^{120}Sn nuclei with the results obtained using NUSHELLX code is presented. From this last table a reasonable agreement between the theoretical and experimental spectra can be seen.

For both projectile and target, Woods-Saxon form factors with reduced radii $r_0 = 1.2$ fm and diffuseness $a_0 = 0.65$ fm were used to obtain single-particle wave functions. The depth of the potentials was varied to fit the experimental neutron binding energies. The spin-orbital interaction was also included with a standard depth of 7 MeV and the same reduced radius and diffuseness as in the case of the scalar potential.

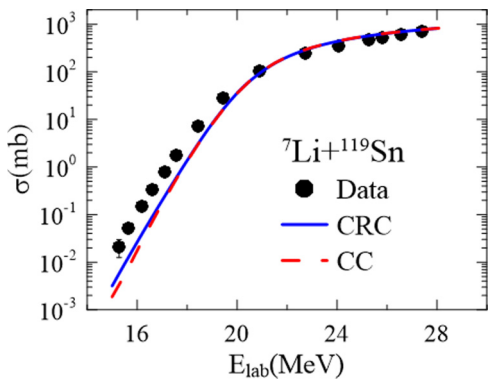

FIG. 14. Comparison of the experimental CF cross sections for the ^{7}Li + ^{119}Sn system with the results obtained from CC and CRC calculations.

The full curve in Fig. 14 shows the results of our CRC calculation in comparison with the CC calculation that does not include the $1n$ transfer channel (dashed curve in Fig. 14). One can see that, for the ^{7}Li induced reaction, which has a larger n-transfer Q value when compared with the ^{6}Li induced collision, the effect of the $1n$ transfer channel is almost negligible, except for the lowest energy points, and this might explain why no differences are observed for the two systems.

VI. SUMMARY AND CONCLUSIONS

This paper presents measurements of CF cross sections for the two reactions ^{6}Li + ^{120}Sn and ^{7}Li + ^{119}Sn, over a Li projectile c.m. energy range from 14 to 28 MeV. The objective of the experiment was to compare the influence of projectile breakup and neutron transfer on the magnitude of the CF cross sections for the two reactions. To emphasise the influence of these two mechanisms, these reactions were chosen since the compound nucleus for both was ^{126}I, and the two heavy target nuclei have similar deformation characteristics. In the energy range investigated, the compound nucleus, ^{126}I, decays predominately by neutron emission to other iodine isotopes. The yields of the isotopes produced were determined by measuring the x-ray residual activity following target bombardment by the lithium beam. The extraction of the CF excitation function from the activity yields was undertaken using the new procedure described in [51]. This procedure is particularly useful to follow when thick targets or poor quality beams are used. For the experiment reported here, good quality stable beams and thin targets were used, so this new procedure produced results close to the ones obtained by using more traditional analysis methods.

The measured cross sections and projectile bombarding energies were reduced to eliminate differences due to trivial static effects and inelastic excitations to bound states. These reduced cross sections and energies were then compared to the universal fusion function according to the prescriptions [25,26]. The renormalized experimental cross sections above the Coulomb barrier fall below the values of the UFF. The suppression factor for ^{6}Li + ^{120}Sn is 0.7 ± 0.05, and for ^{7}Li + ^{119}Sn it is 0.85 ± 0.05. These factors are a little smaller than the ones obtained with heavier targets, so it would be most interesting to undertake measurements of these factors for a wide range of target masses. However, undertaking such an experimental survey is difficult since for lighter targets CF and ICF cannot be easily separated due to charged particle evaporation.

Below the Coulomb barrier, the renormalized experimental cross sections are enhanced relative to the UFF by similar amounts for the two reactions. Such an enhancement, reported also in previous measurements (see as example [25,26,28] and references therein), was attributed to coupling to those channels left out in the CC calculations used to renormalize the data, for example breakup and neutron transfer.

The reduced fusion excitation functions, shown in Fig. 11, for the two reactions ^{6}Li + ^{120}Sn and ^{7}Li + ^{119}Sn, show little

differences even though the Q values for neutron transfer are substantially different. In addition, a CRC calculation has been undertaken for the ^{7}Li + ^{119}Sn reaction, which not only accounts for inelastic scattering but also neutron transfer. This calculation shows that in this particular case, neutron transfer has a negligible effect on the fusion excitation function in the investigated energy range. This suggests that the observed sub-barrier enhancement with respect to the UFF may be due to inelastic excitations of the projectile to the continuum for the considered system, for which there will be large overlaps between projectile and target wave functions. Nevertheless, for more neutron rich projectiles, neutron transfer could still strongly influence fusion.

In order to gain a more complete understanding of how neutron transfer Q value influences fusion, an interesting possibility, being considering by the authors, is to extend the current experiment to investigate the reactions ^{8}Li + ^{118}Sn, ^{9}Li + ^{117}Sn, and even ^{11}Li + ^{115}Sn. The compound nucleus for these reactions is again ^{126}I, but the Q values for one- and two-neutron transfers are very different for the different reactions, as shown in Table I. These experiments will require the use of radioactive beams and thick targets. When these types of experiments are undertaken in the future, the present authors strongly recommend that the extraction of the experimental excitation function, from the raw data, should follow a procedure similar to that used for these currently reported experiments. This is essential to ensure that the beam energy dispersion effects inside targets, due to a combination of the quality of the radioactive beam and straggling in thick targets, can be correctly accounted for, deducing the true excitation function.

ACKNOWLEDGMENTS

A.C.S. acknowledges with gratitude INFN for travel and subsistence support during this work. J.L. and J.F. thank the CNPq and CAPES for their financial support.

[1] M. Beckerman, Rep. Prog. Phys. **51**, 1047 (1988).
[2] B. B. Back, H. Esbensen, C. L. Jiang, and K. E. Rehm, Rev. Mod. Phys. **86**, 317 (2014).
[3] L. Canto, P. Gomes, R. Donangelo, and M. Hussein, Phys. Rep. **424**, 1 (2006).
[4] L. Canto, P. Gomes, R. Donangelo, J. Lubian, and M. Hussein, Phys. Rep. **596**, 1 (2015).
[5] M. Dasgupta, D. J. Hinde, N. Rowley, and A. M. Stefanini, Annu. Rev. Nucl. Part. Sci. **48**, 401 (1998).
[6] N. Rowley, G. Satchler, and P. Stelson, Phys. Lett. B **254**, 25 (1991).
[7] P. H. Stelson, H. J. Kim, M. Beckerman, D. Shapira, and R. L. Robinson, Phys. Rev. C **41**, 1584 (1990).
[8] R. A. Broglia, C. H. Dasso, S. Landowne, and A. Winther, Phys. Rev. C **27**, 2433 (1983).
[9] V. I. Zagrebaev, Phys. Rev. C **67**, 061601 (2003).
[10] S. Kalkal, S. Mandal, N. Madhavan, E. Prasad, S. Verma, A. Jhingan, R. Sandal, S. Nath, J. Gehlot, B. R. Behera, M. Saxena, S. Goyal, D. Siwal, R. Garg, U. D. Pramanik, S. Kumar, T. Varughese, K. S. Golda, S. Muralithar, A. K. Sinha, and R. Singh, Phys. Rev. C **81**, 044610 (2010).
[11] H. Q. Zhang, C. J. Lin, F. Yang, H. M. Jia, X. X. Xu, Z. D. Wu, F. Jia, S. T. Zhang, Z. H. Liu, A. Richard, and C. Beck, Phys. Rev. C **82**, 054609 (2010).
[12] A. M. Stefanini, D. Ackermann, L. Corradi, J. H. He, G. Montagnoli, S. Beghini, F. Scarlassara, and G. F. Segato, Phys. Rev. C **52**, R1727 (1995).
[13] M. Trotta, A. M. Stefanini, L. Corradi, A. Gadea, F. Scarlassara, S. Beghini, and G. Montagnoli, Phys. Rev. C **65**, 011601 (2001).
[14] H. A. Aljuwair, R. J. Ledoux, M. Beckerman, S. B. Gazes, J. Wiggins, E. R. Cosman, R. R. Betts, S. Saini, and O. Hansen, Phys. Rev. C **30**, 1223 (1984).
[15] H. Timmers, D. Ackermann, S. Beghini, L. Corradi, J. He, G. Montagnoli, F. Scarlassara, A. Stefanini, and N. Rowley, Nucl. Phys. A **633**, 421 (1998).
[16] J. J. Kolata, A. Roberts, A. M. Howard, D. Shapira, J. F. Liang, C. J. Gross, R. L. Varner, Z. Kohley, A. N. Villano, H. Amro, W. Loveland, and E. Chavez, Phys. Rev. C **85**, 054603 (2012).
[17] Z. Kohley, J. F. Liang, D. Shapira, R. L. Varner, C. J. Gross, J. M. Allmond, A. L. Caraley, E. A. Coello, F. Favela, K. Lagergren, and P. E. Mueller, Phys. Rev. Lett. **107**, 202701 (2011).
[18] H. M. Jia, C. J. Lin, F. Yang, X. X. Xu, H. Q. Zhang, Z. H. Liu, L. Yang, S. T. Zhang, P. F. Bao, and L. J. Sun, Phys. Rev. C **86**, 044621 (2012).
[19] A. Stefanini, G. Montagnoli, F. Scarlassara, C. Jiang, H. Esbensen, E. Fioretto, L. Corradi, B. Back, C. Deibel, B. Giovine, J. Greene, H. Henderson, S. Marley, M. Notani, N. Patel, K. Rehm, D. Sewerinyak, X. Tang, C. Ugalde, and S. Zhu, Eur. Phys. J. A **49**, 1 (2013).
[20] H. M. Jia, C. J. Lin, F. Yang, X. X. Xu, H. Q. Zhang, Z. H. Liu, Z. D. Wu, L. Yang, N. R. Ma, P. F. Bao, and L. J. Sun, Phys. Rev. C **89**, 064605 (2014).
[21] V. V. Sargsyan, G. G. Adamian, N. V. Antonenko, W. Scheid, and H. Q. Zhang, Phys. Rev. C **85**, 024616 (2012).
[22] V. V. Sargsyan, G. G. Adamian, N. V. Antonenko, W. Scheid, and H. Q. Zhang, Phys. Rev. C **91**, 014613 (2015).
[23] V. A. Rachkov, A. V. Karpov, A. S. Denikin, and V. I. Zagrebaev, Phys. Rev. C **90**, 014614 (2014).
[24] M. Dasgupta, P. R. S. Gomes, D. J. Hinde, S. B. Moraes, R. M. Anjos, A. C. Berriman, R. D. Butt, N. Carlin, J. Lubian, C. R. Morton, J. O. Newton, and A. Szanto de Toledo, Phys. Rev. C **70**, 024606 (2004).
[25] L. F. Canto, P. R. S. Gomes, J. Lubian, L. C. Chamon, and E. Crema, J. Phys. G: Nucl. Part. Phys. **36**, 015109 (2009).
[26] L. Canto, P. Gomes, J. Lubian, L. Chamon, and E. Crema, Nucl. Phys. A **821**, 51 (2009).
[27] P. Gomes, D. M. Junior, L. Canto, J. Lubian, and P. Faria, Few-Body Syst. **57**, 205 (2016).
[28] B. Wang, W.-J. Zhao, P. R. S. Gomes, E.-G. Zhao, and S.-G. Zhou, Phys. Rev. C **90**, 034612 (2014).
[29] S. Santra, S. Kailas, K. Ramachandran, V. V. Parkar, V. Jha, B. J. Roy, and P. Shukla, Phys. Rev. C **83**, 034616 (2011).

[30] J. Lubian, T. Correa, B. Paes, J. Figueira, D. Abriola, J. F. Niello, A. Arazi, O. Capurro, E. de Barbar, G. Mart, D. M. Heinmann, A. Negri, A. Pacheco, I. Padron, and P. Gomes, Nucl. Phys. A **791**, 24 (2007).
[31] W. Y. So, K. S. Kim, K. S. Choi, and M.-K. Cheoun, Phys. Rev. C **90**, 054615 (2014).
[32] D. R. Otomar, J. Lubian, P. R. S. Gomes, and T. Correa, J. Phys. G: Nucl. Part. Phys. **40**, 125105 (2013).
[33] R. Rafiei, R. du Rietz, D. H. Luong, D. J. Hinde, M. Dasgupta, M. Evers, and A. Diaz-Torres, Phys. Rev. C **81**, 024601 (2010).
[34] D. Luong, M. Dasgupta, D. Hinde, R. du Rietz, R. Rafiei, C. Lin, M. Evers, and A. Diaz-Torres, Phys. Lett. B **695**, 105 (2011).
[35] D. H. Luong, M. Dasgupta, D. J. Hinde, R. du Rietz, R. Rafiei, C. J. Lin, M. Evers, and A. Diaz-Torres, Phys. Rev. C **88**, 034609 (2013).
[36] E. C. Simpson, K. J. Cook, D. H. Luong, S. Kalkal, I. P. Carter, M. Dasgupta, D. J. Hinde, and E. Williams, Phys. Rev. C **93**, 024605 (2016).
[37] M. M. Shaikh, S. Roy, S. Rajbanshi, M. K. Pradhan, A. Mukherjee, P. Basu, S. Pal, V. Nanal, R. G. Pillay, and A. Shrivastava, Phys. Rev. C **90**, 024615 (2014).
[38] M. M. Shaikh, S. Roy, S. Rajbanshi, A. Mukherjee, M. K. Pradhan, P. Basu, V. Nanal, S. Pal, A. Shrivastava, S. Saha, and R. G. Pillay, Phys. Rev. C **93**, 044616 (2016).
[39] H. Kumawat, V. Jha, V. V. Parkar, B. J. Roy, S. K. Pandit, R. Palit, P. K. Rath, C. S. Palshetkar, S. K. Sharma, S. Thakur, A. K. Mohanty, A. Chatterjee, and S. Kailas, Phys. Rev. C **86**, 024607 (2012).
[40] A. Di Pietro, P. Figuera, F. Amorini, C. Angulo, G. Cardella, S. Cherubini, T. Davinson, D. Leanza, J. Lu, H. Mahmud, M. Milin, A. Musumarra, A. Ninane, M. Papa, M. G. Pellegriti, R. Raabe, F. Rizzo, C. Ruiz, A. C. Shotter, N. Soić, S. Tudisco, and L. Weissman, Phys. Rev. C **69**, 044613 (2004).
[41] A. Di Pietro, Eur. Phys. J.: Spec. Top. **150**, 15 (2007).
[42] V. Scuderi, A. Di Pietro, P. Figuera, M. Fisichella, F. Amorini, C. Angulo, G. Cardella, E. Casarejos, M. Lattuada, M. Milin, A. Musumarra, M. Papa, M. G. Pellegriti, R. Raabe, F. Rizzo, N. Skukan, D. Torresi, and M. Zadro, Phys. Rev. C **84**, 064604 (2011).
[43] A. Di Pietro, P. Figuera, E. Strano, M. Fisichella, O. Goryunov, M. Lattuada, C. Maiolino, C. Marchetta, M. Milin, A. Musumarra, V. Ostashko, M. G. Pellegriti, V. Privitera, G. Randisi, L. Romano, D. Santonocito, V. Scuderi, D. Torresi, and M. Zadro, Phys. Rev. C **87**, 064614 (2013).
[44] J. J. Kolata, V. Guimarães, D. Peterson, P. Santi, R. White-Stevens, P. A. DeYoung, G. F. Peaslee, B. Hughey, B. Atalla, M. Kern, P. L. Jolivette, J. A. Zimmerman, M. Y. Lee, F. D. Becchetti, E. F. Aguilera, E. Martinez-Quiroz, and J. D. Hinnefeld, Phys. Rev. Lett. **81**, 4580 (1998).
[45] P. A. DeYoung, B. Hughey, P. L. Jolivette, G. F. Peaslee, J. J. Kolata, V. Guimarães, D. Peterson, P. Santi, H. C. Griffin, J. A. Zimmerman, and J. D. Hinnefeld, Phys. Rev. C **58**, 3442 (1998).
[46] C. Signorini, A. Yoshida, Y. Watanabe, D. Pierroutsakou, L. Stroe, T. Fukuda, M. Mazzocco, N. Fukuda, Y. Mizoi, M. Ishihara, H. Sakurai, A. Diaz-Torres, and K. Hagino, Nucl. Phys. A **735**, 329 (2004).
[47] Y. E. Penionzhkevich, V. I. Zagrebaev, S. M. Lukyanov, and R. Kalpakchieva, Phys. Rev. Lett. **96**, 162701 (2006).
[48] Y. Penionzhkevich, R. Astabatyan, N. Demekhina, G. Gulbekian, R. Kalpakchieva, A. Kulko, S. Lukyanov, E. Markaryan, V. Maslov, Y. Muzychka, Y. Oganessian, R. Revenko, N. Skobelev, Y. Sobolev, D. A. Testov, and T. Zholdybaev, Eur. Phys. J. A **31**, 185 (2007).
[49] A. Lemasson, A. Shrivastava, A. Navin, M. Rejmund, N. Keeley, V. Zelevinsky, S. Bhattacharyya, A. Chatterjee, G. de France, B. Jacquot, V. Nanal, R. G. Pillay, R. Raabe, and C. Schmitt, Phys. Rev. Lett. **103**, 232701 (2009).
[50] R. Wolski, I. Martel, Ł. Standłyo, L. Acosta, J. Aguado, C. Angulo, R. Berjillos, J. Bolivar, J. Duenas, M. Golovkov, T. Keutgen, M. Mazzocco, A. Padilla, A. Sánchez-Benítez, C. Signorini, M. Romoli, and K. Rusek, Eur. Phys. J. A **47**, 111 (2011).
[51] M. Fisichella, A. C. Shotter, A. Di Pietro, P. Figuera, M. Lattuada, C. Marchetta, V. Privitera, L. Romano, C. Ruiz, and M. Zadro, Phys. Rev. C **92**, 064611 (2015).
[52] M. Fisichella, Ph.D. thesis, Universitá di Messina, 2013 (unpublished), http://www.infn.it/thesis/index.php.
[53] F. Pühlhofer, Nucl. Phys. A **280**, 267 (1977).
[54] National Nuclear Data Center, Brookhaven National Laboratory, Upton, NY, http://www.nndc.bnl.gov/.
[55] J. Ziegler, M. Ziegler, and J. Biersack, Nucl. Instrum Methods B **268**, 1818 (2010).
[56] J. Ziegler, SRIM code, http://www.srim.org/.
[57] P. Bevington and D. Robinson, *Data Reduction and Error Analysis for the Physical Sciences*, 3rd ed. (Mc Graw-Hill, New York, 2003).
[58] F. James and M. Roos, Comput. Phys. Commun. **10**, 343 (1975).
[59] C. Y. Wong, Phys. Rev. Lett. **31**, 766 (1973).
[60] I. J. Thompson, Comput. Phys. Rep. **7**, 167 (1988).
[61] S. Raman, C. Nestor, and P. Tikkanen, At. Data Nucl. Data Tables **78**, 1 (2001).
[62] L. C. Chamon, D. Pereira, M. S. Hussein, M. A. Cândido Ribeiro, and D. Galetti, Phys. Rev. Lett. **79**, 5218 (1997).
[63] L. C. Chamon, B. V. Carlson, L. R. Gasques, D. Pereira, C. De Conti, M. A. G. Alvarez, M. S. Hussein, M. A. Cândido Ribeiro, E. S. Rossi, and C. P. Silva, Phys. Rev. C **66**, 014610 (2002).
[64] P. R. S. Gomes, J. Lubian, and L. F. Canto, Phys. Rev. C **79**, 027606 (2009).
[65] L. F. Canto, P. R. S. Gomes, J. Lubian, M. S. Hussein, and P. Lotti, Eur. Phys. J. A **50**, 1 (2014).
[66] S. P. Hu, G. L. Zhang, J. C. Yang, H. Q. Zhang, P. R. S. Gomes, J. Lubian, X. G. Wu, J. Zhong, C. Y. He, Y. Zheng, C. B. Li, G. S. Li, W. W. Qu, F. Wang, L. Zheng, L. Yu, Q. M. Chen, P. W. Luo, H. W. Li, Y. H. Wu, W. K. Zhou, B. J. Zhu, and H. B. Sun, Phys. Rev. C **91**, 044619 (2015).
[67] L. R. Gasques, D. J. Hinde, M. Dasgupta, A. Mukherjee, and R. G. Thomas, Phys. Rev. C **79**, 034605 (2009).
[68] W. Rae, NuShellX, http://garsington.eclipse.co.uk/.
[69] S. Cohen and D. Kurath, Nucl. Phys. **73**, 1 (1965).
[70] B. A. Brown, N. J. Stone, J. R. Stone, I. S. Towner, and M. Hjorth-Jensen, Phys. Rev. C **71**, 044317 (2005).